JCI The Journal of Clinical Investigation

Real-time imaging of de novo arteriovenous malformation in a mouse model of hereditary hemorrhagic telangiectasia

Sung Ok Park, … , Brian S. Sorg, S. Paul Oh

J Clin Invest. 2009;119(11):3487-3496. https://doi.org/10.1172/JCI39482.

Technical Advance **Vascular biology**

Arteriovenous malformations (AVMs) are vascular anomalies where arteries and veins are directly connected through a complex, tangled web of abnormal arteries and veins instead of a normal capillary network. AVMs in the brain, lung, and visceral organs, including the liver and gastrointestinal tract, result in considerable morbidity and mortality. AVMs are the underlying cause of three major clinical symptoms of a genetic vascular dysplasia termed hereditary hemorrhagic telangiectasia (HHT), which is characterized by recurrent nosebleeds, mucocutaneous telangiectases, and visceral AVMs and caused by mutations in one of several genes, including activin receptor–like kinase 1 (*ALK1*). It remains unknown why and how selective blood vessels form AVMs, and there have been technical limitations to observing the initial stages of AVM formation. Here we present in vivo evidence that physiological or environmental factors such as wounds in addition to the genetic ablation are required for Alk1-deficient vessels to develop to AVMs in adult mice. Using the dorsal skinfold window chamber system, we have demonstrated for what we believe to be the first time the entire course of AVM formation in subdermal blood vessels by using intravital bright-field images, hyperspectral imaging, fluorescence recordings of direct arterial flow through the AV shunts, and vascular casting techniques. We believe our data provide novel insights into the pathogenetic mechanisms of HHT and potential therapeutic approaches.

Real-time imaging of de novo arteriovenous malformation in a mouse model of hereditary hemorrhagic telangiectasia

Sung Ok Park,[1,2] Mamta Wankhede,[3] Young Jae Lee,[1,4] Eun-Jung Choi,[1,2] Naime Fliess,[1,2] Se-Woon Choe,[3] Seh-Hoon Oh,[5] Glenn Walter,[1] Mohan K. Raizada,[1] Brian S. Sorg,[3] and S. Paul Oh[1,2,4]

[1]Department of Physiology and Functional Genomics, College of Medicine, [2]University of Florida Shands Cancer Center, and [3]J. Crayton Pruitt Family Department of Biomedical Engineering, College of Engineering, University of Florida, Gainesville, Florida, USA. [4]Lee Gil Ya Cancer and Diabetes Institute, Gachon University of Medicine and Science, Incheon, Republic of Korea. [5]Department of Pathology, Immunology and Laboratory Medicine, College of Medicine, University of Florida, Gainesville, Florida, USA.

Arteriovenous malformations (AVMs) are vascular anomalies where arteries and veins are directly connected through a complex, tangled web of abnormal arteries and veins instead of a normal capillary network. AVMs in the brain, lung, and visceral organs, including the liver and gastrointestinal tract, result in considerable morbidity and mortality. AVMs are the underlying cause of three major clinical symptoms of a genetic vascular dysplasia termed hereditary hemorrhagic telangiectasia (HHT), which is characterized by recurrent nosebleeds, mucocutaneous telangiectases, and visceral AVMs and caused by mutations in one of several genes, including activin receptor–like kinase 1 (*ALK1*). It remains unknown why and how selective blood vessels form AVMs, and there have been technical limitations to observing the initial stages of AVM formation. Here we present in vivo evidence that physiological or environmental factors such as wounds in addition to the genetic ablation are required for Alk1-deficient vessels to develop to AVMs in adult mice. Using the dorsal skinfold window chamber system, we have demonstrated for what we believe to be the first time the entire course of AVM formation in subdermal blood vessels by using intravital bright-field images, hyperspectral imaging, fluorescence recordings of direct arterial flow through the AV shunts, and vascular casting techniques. We believe our data provide novel insights into the pathogenetic mechanisms of HHT and potential therapeutic approaches.

Introduction

Arteriovenous malformation (AVM) refers to a vascular anomaly wherein arteries and veins are directly connected through a complex, tangled web of abnormal arteries and veins by one or more fistulas (abnormal communications) instead of a normal capillary network. Blood vessels in AVM lesions appear to be dilated, with thin vessel walls that are prone to rupture and cause hemorrhages. AVMs are found in the brain, spinal cord, lung, and visceral organs such as liver, gastrointestinal (GI) tract, and spleen. About 300,000 Americans are estimated to have an AVM (1). Most people with an AVM do not develop any symptoms, but about 12% of those affected may develop significant symptoms (1). Symptoms of brain AVM include headache, seizures, and hemorrhages leading to stroke. Pulmonary AVMs can lead to transient ischemic attack, embolic stroke, brain abscesses, and hemoptysis. Pathogenetic mechanisms underlying AVM development are largely unknown.

Hereditary hemorrhagic telangiectasia (HHT), also known as Osler-Weber-Rendu syndrome, is a genetic disorder of blood vessels inherited as an autosomal dominant trait with a prevalence of approximately 1:5,000 to 1:10,000 (2, 3). A person is diagnosed with HHT when he/she possesses at least 3 of the 4 Curaçao criteria: (a) an affected immediate family member, (b) recurrent nosebleeds, (c) multiple telangiectasias along the mucocutaneous surface, and (d) AVMs on major organs (2). The underlying cause of the major clinical symptoms of HHT is abnormal connections between arteries and veins. Therefore, HHT is a unique genetic vascular disease, the study of which may elucidate fundamental pathophysiological mechanisms of AVM.

Life-threatening conditions of HHT patients often result from AVMs in the major organs, such as brain and lung. Rapid advances in genetic diagnosis and interventional radiological techniques allow life-threatening AVMs of HHT patients to be detected in the early stage of life and treated, even though invasive procedures are still required. The area in which improvements in HHT therapy are most needed is controlling nosebleed, GI bleeding, and diffused AVMs. Nosebleeds and GI bleedings are largely due to small AVMs (telangiectases) that form in the nasal layer of skin and GI tract, respectively. More than 90% of HHT patients experience recurrent nose bleeding (average 9 times a week), a heavy burden because it inhibits social activities, causes anemia, occurs throughout life, and gets worse with age (4). Even though many interventional techniques are being developed (5, 6), these are only temporary solutions, and drugs that can promote blood clots are the only therapeutic methods that show a limited success in ameliorating nosebleeds or GI bleeding. Novel therapy for preventing AVM formation based on disease mechanisms is greatly needed for HHT patients.

Clinically indistinguishable forms of HHT arise from mutations in at least 5 autosomal genes. HHT types 1 and 2 are due to heterozygous mutations in endoglin (*ENG*) and activin receptor–like kinase 1 (*ACVRL1*; *ALK1*), respectively (3, 7, 8). Recently, 2 other genetic loci on chromosomes 5 and 7 were mapped for HHT3 and HHT4, respectively (9, 10). Identification of causative genes from these 2 loci will aid in our understanding of molecular basis of

Conflict of interest: The authors have declared that no conflict of interest exists.
Citation for this article: *J. Clin. Invest.* **119**:3487–3496 (2009). doi:10.1172/JCI39482.

HHT. A subset of HHT patients has a combined syndrome of HHT and juvenile polyposis (JP). These JP-HHT patients have a mutation in the SMAD4 (*MADH4*) gene (11). Interestingly, all of 3 identified genes associated with HHT are components of signal transduction of TGF-β family members; thus, HHT has been considered a disease caused by defects in signaling of a TGF-β family member (12).

Although the genes that cause HHT have been known for over a decade, mechanisms that underlie HHT pathogenesis remain obscure. An intriguing feature of HHT is variability of disease manifestations. Even among kin, the severity, age of onset, and locations of the vascular lesions are extremely variable from one individual to another (13). In addition, only select vascular beds develop telangiectasis or AVM lesions, while other such areas remain normal in an HHT patient (14). Therefore, it has been postulated that other physiological, environmental or genetic factors ("second hits") in addition to the haploinsufficiency (reduced functional protein) of *ALK1* or *ENG* are involved in the development of vascular lesions in HHT patients. However, the requirement of a second hit in the development of AVM has not been experimentally proven. Another important step toward understanding HHT pathogenesis is development of a model system that allows observation of the birth and growth of AVMs in real time.

In this article, utilizing the $Alk1^{2loxP}$ allele and endothelium-specific and tamoxifen-inducible (TM-inducible) Cre drivers (15–17), we present what we believe to be novel neonatal and adult mouse models that reproduce clinical HHT vascular lesions in a robust, consistent, and predictable manner. We provide evidence that wounding is a second hit essential for de novo AVM formation in *Alk1*-deficient subdermal vasculatures in adult stages. In addition, we present, for the first time to our knowledge, a real-time observation of developing functional AVM formations in adult mice. It is hoped that these mouse models coupled with intravital microscopy for real-time serial imaging in the same individual mice will be valuable resources to further study the mechanisms underlying generation of AVMs acquired in developmental and adult stages and for models for testing various potential drugs to inhibit AVM formation or to induce regression of AVMs.

Results

Endothelial ALK1 is essential for the establishment of proper AV connections during development. Deletion of the *Alk1* gene from the $Alk1^{2loxP}$ allele with the EC-specific L1Cre line (15) resulted in postnatal lethality. All L1Cre(+);$Alk1^{2loxP/2loxP}$ mice ($n > 60$) had characteristic vascular phenotypes as described below or were found dead by P5, with hemorrhages in the brain, lung, and GI tract. Blood vessels in the superficial layer of these organs appeared to be dilated, disorganized, and tortuous (Figure 1, G and M, Supplemental Figure 1B, and Supplemental Figure 2B; supplemental material available online with this article; doi:10.1172/JCI39482DS1). A right or left ventricular injection of latex dye, corrosion cast, or Evans blue dye was used to visualize gross morphology and arteriovenous (AV) connections of the blood vessels within these organs. The latex dye did not cross the capillary beds and was retained within the arterial branches in the control organs. As shown in Figure 1, A and C, the latex dye highlighted major arterial branches in the brain of control mice. In the mutants, however, the latex dye was found in the venous as well as arterial branches (Figure 1, B, D, and E), indicating the presence of AV shunts. The morphology and pattern of blood vessels visualized by latex dye in the mutants were strikingly different from those in the controls. The mutant vessels showed peculiar looping at the distal tip of blood vessels (Figure 1, D and E). A higher-magnification view revealed that these looping vessels consisted of numerous AV fistulas (Figure 1E). Corrosion casting, histological sections, and 3D reconstruction images by magnetic resonance (MR) demonstrated dilated and hemorrhagic vessels in various brain areas, including the hippocampus (Supplemental Figure 1, C–F, and Supplemental Videos 1 and 2). The mutant lungs also manifested numerous blood vessels with abnormal morphology and AV connections similar to those in the mutant brain. Dilated, convoluted, and tortuous vessels with signs of hemorrhage were often observed in the superficial layer of the lung (Figure 1G and Supplemental Figure 2B). The Evans blue dye injection highlighted such bulged, tortuous vessels on the surface of the lung (Figure 1I). Corrosion casting followed by scanning electron micrography also demonstrated the peculiar pattern of abnormal looping vessels similar to the ones in the brain (Figure 1K). The latex dye injection showed AV shunting and diminished perfusion to distal microvessels in the mutant lung (Supplemental Figure 2, C–F). Histological sections demonstrated dilated, irregular, and disorganized vessels with uneven and discontinuous smooth muscle layers (Supplemental Figure 2, G–J). The Evans blue dye appeared to be diffused and was found in airways, indicating highly permeable and leaky vessels in the mutants (Supplemental Figure 2L). As in the brain and lungs, dilated, tortuous, irregular, and disorganized vessels were present in the vasculature of mutant small intestines (Figure 1, L–Q). On the other hand, such vascular abnormalities were not observed in the skin, heart, muscle, kidney, and large intestine (data not shown).

ALK1 in adult mice is essential for vascular homeostasis in small intestinal, pulmonary, and uterine vessels. To investigate the role of ALK1 in adult stages (more than 2 months of age) when most blood vessel networks are already established, we globally deleted the *Alk1* gene using the CreER system, in which Cre recombinase can be temporarily activated by administration of TM. We used the ROSA26-CreER knock-in mouse strain ($R26^{+/CreER}$), which ubiquitously expresses CreER (17). TM administration to adult $R26^{+/CreER}Alk1^{2loxP/2loxP}$ mice resulted in lethality 9–21 days after a single TM injection (2.5 mg/25 g BW, i.p.) (Figure 2A). The TM-injected mutant mice displayed signs of illness such as slow movements and weight loss from 8 to 10 days after TM injection. Typically, the mutants displayed pale paws (Figure 2B), low pO_2 levels (Figure 2C), and darkened feces (Figure 2D), indicating internal hemorrhages and anemia. Consistent with these observations, the mutants at 8–10 days after TM injection showed an enlarged heart (Supplemental Figure 3), signs of hemorrhages in the lungs and GI tract (Supplemental Figure 4, B and H), and significantly reduced hematocrit (Figure 2E). Presence of pulmonary AVMs was difficult to assess due to hindrances by hemorrhagic spots, but both pulmonary arteries and veins appeared to be markedly dilated (Supplemental Figure 4, C–F). The surface of the vascular cast was rough, indicating high vascular permeability (Supplemental Figure 4, D and F). Interestingly, most AVMs in the GI tract of the mutants were located in the Peyer's patches of small intestine and appendix (Figure 2, F–H, and Supplemental Figure 4, I–L). The uterus was another organ that showed consistent and strong signs of AVMs (Supplemental Figure 5). These uterine AVMs may be associated with the shorter survival span of TM-treated mutant females than males (Figure 2A).

Wounding can induce de novo AVM formation in Alk1-deficient subdermal vessels during adult stages. While blood vessels of particular

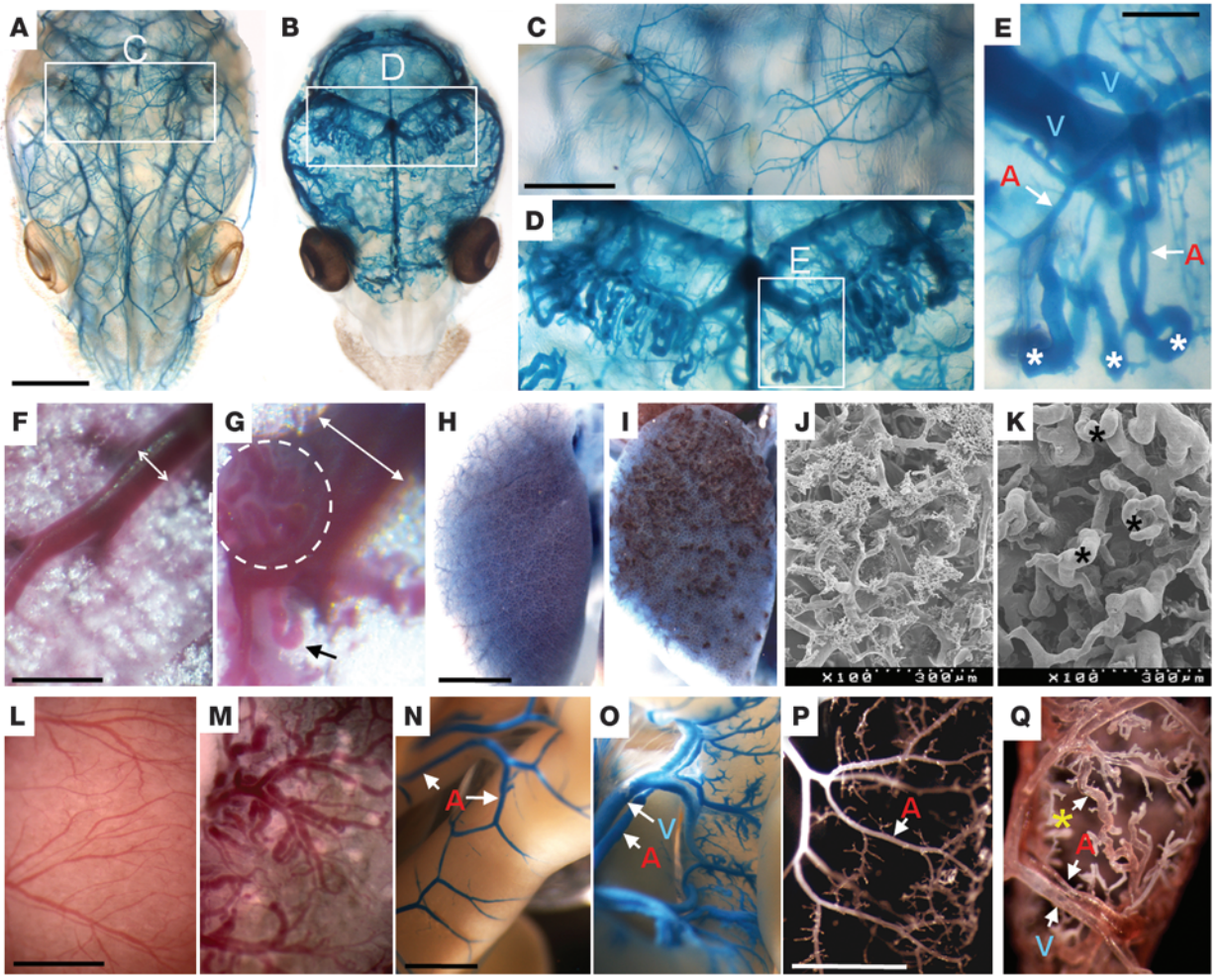

Figure 1
Endothelial *Alk1* deletion from the *Alk1*^{2loxP} allele resulted in postnatal lethality by P5, with AVMs in the brain, lung, and GI tract. (**A**–**E**) Dissection microscopic views of vascular images of control [L1Cre(–);*Alk1*$^{2loxP/2loxP}$; **A** and **C**] and mutant [L1Cre(+);*Alk1*$^{2loxP/2loxP}$; **B**, **D**, and **E**] P3 mouse brains with latex dye injected into the left ventricle of the heart. (**D** and **E**) Magnified views of blood vessels in the hippocampal area. (**E**) Asterisks indicate peculiar looping of vessels at the distal tips of arteries shunting to veins. A, artery; V, vein. (**F**–**K**) Vascular morphology of control (**F**, **H**, and **J**) and mutant (**G**, **I**, and **K**) P3 lungs. (**F** and **G**) Dissection microscopic view of pulmonary veins. Double-headed arrows indicate diameter of pulmonary veins. A dashed circle highlights the area of abnormal tangled vessels, and an arrow indicates looping of a dilated vessel (**G**). (**H** and **I**) Gross views of left lung after Evans blue dye injection via jugular veins. Note bumpy, dilated looping vessels in the mutant lungs (**I**). (**J** and **K**) Scanning electron micrograph view of corrosion cast, showing lack of microvessels and presence of numerous dilated looping vessels (asterisks) in the mutant lungs (**K**). (**L**–**Q**) Gross views of small intestines of control (**L**, **N**, and **P**) and mutant (**M**, **O**, and **Q**) P3 mice. AV shunts and abnormal anastomosis was observed by latex dye (**O**) and corrosion cast (indicated by an arrow with asterisk; **Q**). Scale bars: 2 mm (**A** and **B**); 1 mm (**C**, **D**, **H**, **I**, and **N**–**Q**); 300 μm (**E**); 500 μm (**F**, **G**, **L**, and **M**).

organs such as lung, uterus, and (Peyer's patches of) small intestine were affected, those of other organs including brain and subdermal vessels were unaffected in TM-injected adult *R26*$^{+/CreER}$ *Alk1*$^{2loxP/2loxP}$ mice. This result suggests that there may be some physiological conditions that give rise to expression or function of ALK1 in specific organs in adult stages. We have previously shown that strong Alk1 expression in neonatal stages was suppressed in adult stages, except in certain organs including lungs (18). The suppressed Alk1 expression in adult subdermal blood vessels was shown to be induced in feeding arteries and newly forming blood vessels during wound healing (18). To test the role of ALK1 during wound healing in adult mice, we injected TM in mice bearing excisional wounds on the dorsal skin and ear of control and *R26*$^{+/CreER}$*Alk1*$^{2loxP/2loxP}$ mice. Eight days later, the latex dye was injected via left heart to display vascular connections. Single arterial trees were observed in the TM-treated control mice with wounds (n = 10) (Figure 3, A and C) or in the TM-treated mutant mice without wounds (n = 6) (data not shown). On the other hand, latex dye was present in both arterial and venous branches — appearing as double branches — in the TM-injected mutant mice with wounds (n = 14) (Figure 3, B and D). Direct AV shunts were visualized in the blood vessels near the wounds (Figure 3D, inset). No AV shunts or abnormal vascular morphology such as dilatation or tortuosity were detected on the blood vessels away

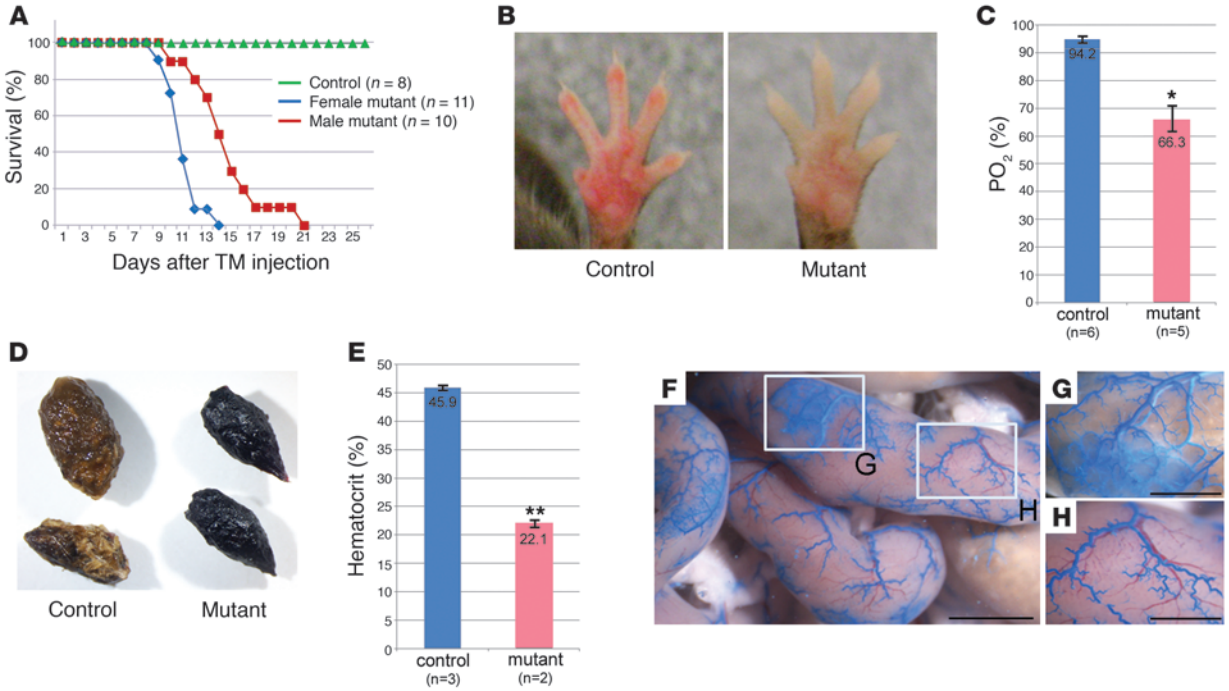

Figure 2

Global *Alk1* deletion in adult stages resulted in lethality with hemorrhages in the lung and GI tract. (**A**) Kaplan-Meier survival curve, showing lethality from *Alk1* deletion in male and female adult mice. Female mice were more sensitive to *Alk1* deletion than males. Control: $R26^{+/+}Alk1^{2loxP/2loxP}$; mutant: $R26^{+/CreER}Alk1^{2loxP/2loxP}$. (**B**–**D**) Mutant mice displayed external signs of internal bleeding and anemia, such as pale paws (**B**), a low pO_2 level (**C**), and darkened feces (**D**) by 8 days after TM injection. (**E**) Reduced hematocrit in the mutants 8 days after TM injection. Error bars in **C** and **E** indicate SD. (**F**–**H**) Superficial blood vessels in the small intestine of the mutant 8 day after TM injecting were visualized by latex dye. Formation of AVM judged by the presence of latex dye in both arteries and veins was apparent in the areas of Peyer's patches (**G**). Scale bars: 4 mm (**F**); 2 mm (**G** and **H**). $^{*}P < 0.05$; $^{**}P < 0.001$.

from the wound, suggesting that this phenomenon is associated with local wound responses. The percentage of blood vessels containing latex dye in the mutant subdermal vessels of the wound area was about 3-fold higher than that in controls (Figure 3, E and F). This difference corresponds to vessel dilatation and AV shunts in the mutant vessels. These data demonstrate that both environmental factors (i.e., wound) and genetic factors (i.e., *Alk1*-homozygous deletion) are required for the formation of AVMs in adult subdermal vessels.

Real-time imaging of de novo AVM development in adult subdermal vessels. As shown above, we were able to demonstrate the formation of de novo AV shunts by latex dye injection. However, we were unable to examine the onset, progression, remodeling, and hemodynamic characters of these AV shunts. To overcome these limitations, we utilized a recently developed hyperspectral imaging system in a dorsal skinfold window chamber model (19–22), which allows monitoring the process of vascular remodeling during wound healing through intravital images. With this system, we obtained bright-field images, levels of hemoglobin (Hb) oxygen saturation, and video recording of blood flow on the blood vessels of control and mutant mice during wound healing for 8 days. As shown in Figure 4, there were remarkable differences in the vascular remodeling between controls and mutants. First, a large number of nascent microvessels formed and grew toward the center of the wound in the controls (Figure 4, A and B), whereas fewer nascent vessels developed, and they continued to remodel at the at the perimeter of the wound in the mutants (Figure 4, C and D). Second, $Hb(O_2)$ saturation levels in the venous vessels remained constant in the controls (Figure 4A), while they were remarkably elevated in the mutant veins during the course of 8 days (Figure 4D and Figure 5H). Third, there were only minor changes in major arterial and venous branches of the controls, while progressive, conspicuous dilation and remodeling of major arterial and venous vessels occurred in the mutants.

An $Hb(O_2)$ saturation map provides evidence of AV shunting in the mutants as early as day 3 (Figure 5B). Dilation of veins connecting to arterial branches was observed by days 4–6 (Figure 5C), followed by marked dilatation of feeding arteries by days 6–8, when patent AV shunts were created (Figure 5, E and F). Numerous vessels appeared to be regressed as stable AV shunts were established. To examine the blood flow in these AVMs, we injected fluorescently labeled rbc into the mice via tail vein and video recorded the flow through the AV shunts at days 7 and 8. At the end of the skin chamber study, we injected the latex dye into the left heart. Consistent with data in Figure 3, only arterial vessels contained the dye in the controls, while both arteries and veins contained dye in the mutants (Figure 6, A and B). As shown in Supplemental Videos 3 and 4 (Figure 6, D and E), arterial blood directly shunted through numerous connecting AV anastomoses (Figure 6C). Blood vessel segments with a dilated and tortuous morphology coincided with areas of high-velocity, turbulent arterial blood flow (Figure 5G and Figure 6C).

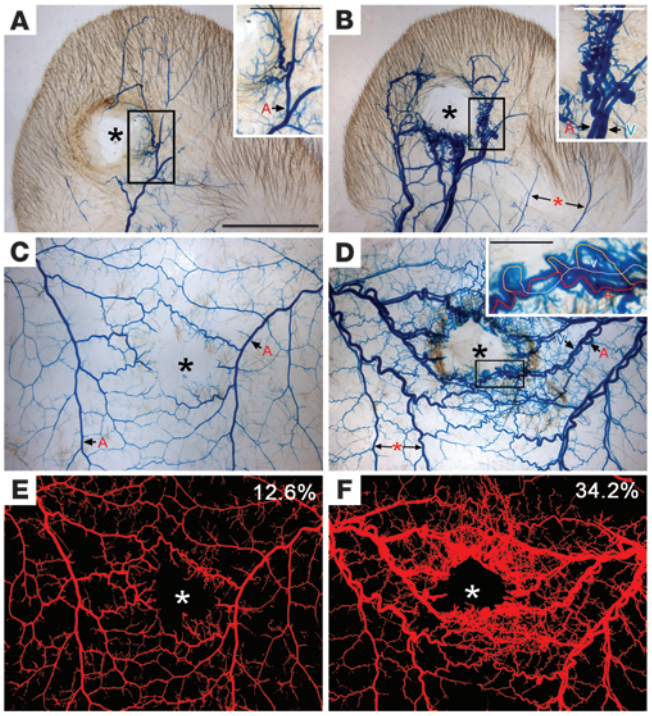

Figure 3
Wounding can induce de novo AVM formation in *Alk1*-deleted adult mice. Vascular patterns shown by latex dye injected into the left heart of control (*R26*$^{+/+}$*Alk1*$^{2loxP/2loxP}$; **A**, **C**, and **E**) and mutant (*R26*$^{+/CreER}$ *Alk1*$^{2loxP/2loxP}$; **B**, **D**, and **F**) mice bearing wounds in the ear (**A** and **B**) or dorsal skin (**C**–**F**), 8 days after TM injection. The images were taken after clearing in organic solvents. The center of the wound is indicated by an asterisk. Note that only mutant mice developed AV shunts, shown by the presence of latex dye in both arteries and veins. AV shunting and abnormal vascular morphologies were apparent only in the wound areas. Blood vessels away from the wound, indicated by arrows with asterisks (**B** and **D**), showed normal appearance. Inset in **D** shows a magnified view of AV fistulas formed in the rim area of the mutant wound. Arteries and veins are marked by red and light blue lines, respectively, and the AV anastomoses by yellow lines. (**E** and **F**) The images in **C** and **D** were processed to quantify the area of blood vessels containing the latex dye in the given area. All figure panels are at the same magnification. Scale bars: 5 mm (**A**); 2 mm (insets in **A** and **B**); 1 mm (inset in **D**).

Discussion

To date, there has been no valid system to observe development and progression of AVM in real time that would provide crucial information about why and how AVMs form. Using the dorsal skinfold window chamber system, we demonstrated for the first time to our knowledge an early stage of AVM formation in adult subdermal blood vessels in real time. In combination with transluminescence, hyperspectral, and fluorescence imaging systems (21, 22), this model allowed us to obtain intravital images of vascular remodeling during AVM formation in the mutants. Specifically, we obtained (a) bright-field microscopic images of blood vessels, (b) levels of Hb saturation at any vessel segments (for visual detection of AV shunting), and (c) video recording of blood flow on normal and AVM vessels. This window chamber model is highly reproducible, easy to manipulate, and a relevant model system for studying pathogenesis of skin AVMs (telangiectasia).

Our imaging data show that AVM formation involves active extension of arterial blood vessels that meet with growing venous branches. Hemorrhages accompany with the initial stages of AV connections. A complex remodeling process is involved in shaping an AVM, and hemodynamic conditions seem to play an important role in this process. Numerous AV anastomoses were found in an AVM lesion. Some studies have indicated that blood vessel dilation is a cause of AVM (23, 24). High-velocity, turbulent arterial blood flow through these anastomosis resulted in dilatation and tortuosity of vessel morphology. Our time course data showed that contact between arterial and venous vessels preceded dilation of postcapillary venules followed by remodeling of arterial vessels, suggesting that dilatation of arterial and venous vessels is a consequence rather than a cause of or a risk factor for AV shunts. Addition of deep-penetrating and noninvasive multiphoton fluorescence microscopy (25–28) to this window chamber model would allow us to capture high-resolution 3D time-lapse images during AVM formation at a subcellular level and greatly facilitate our understanding of the progression of AVM formations.

Only select vascular beds in an HHT patient develop telangiectasis or AVM lesions, while other areas (>99.9%) remain normal (14). Therefore, it has been postulated that other physiological or environmental factors (or second hits), in addition to the genetic predisposition by ENG or ALK1 mutations, must be involved in the development of vascular malformations in HHT patients. We have shown that *Alk1* deletion resulted in de novo AVM formations in subdermal blood vessels only in the area where a wound was created. This is the first experimental in vivo evidence to our knowledge demonstrating that a second hit is indeed essential for the development of de novo AVMs in HHT, and that wounding or wound response can serve as such a second hit. This result provides clinical insights relevant for understanding the pathogenetic mechanism underlying skin telangiectasia and nosebleeds, the most prevalent symptoms of HHT. Telangiectasia occurs most frequently in the nasal cavity and in areas of the mouth in HHT patients, perhaps because these are highly vascularized tissues that are in constant contact with the external environment and subject to chronic inflammation, infections, or injuries that induce a reaction similar to the wound response.

Our data suggest 2 overall strategies for development of a therapy for nosebleeds: either compensation of the ALK1 deficiency or inhibition of critical pathways responding to the second hit can prevent the de novo AVM formation. Identification of downstream effector genes of ALK1 signaling pertinent to AVM formation would be extremely beneficial for discovering new therapeutic targets for overcoming ALK1 deficiency. On the other hand, understanding the nature of second hits and identifying crucial mediators of the second hit would provide another important key for the development of therapeutics for HHT.

From our skin AVM studies, we identified wounding as a second hit. Wounds generate multiple, complex signals for its healing

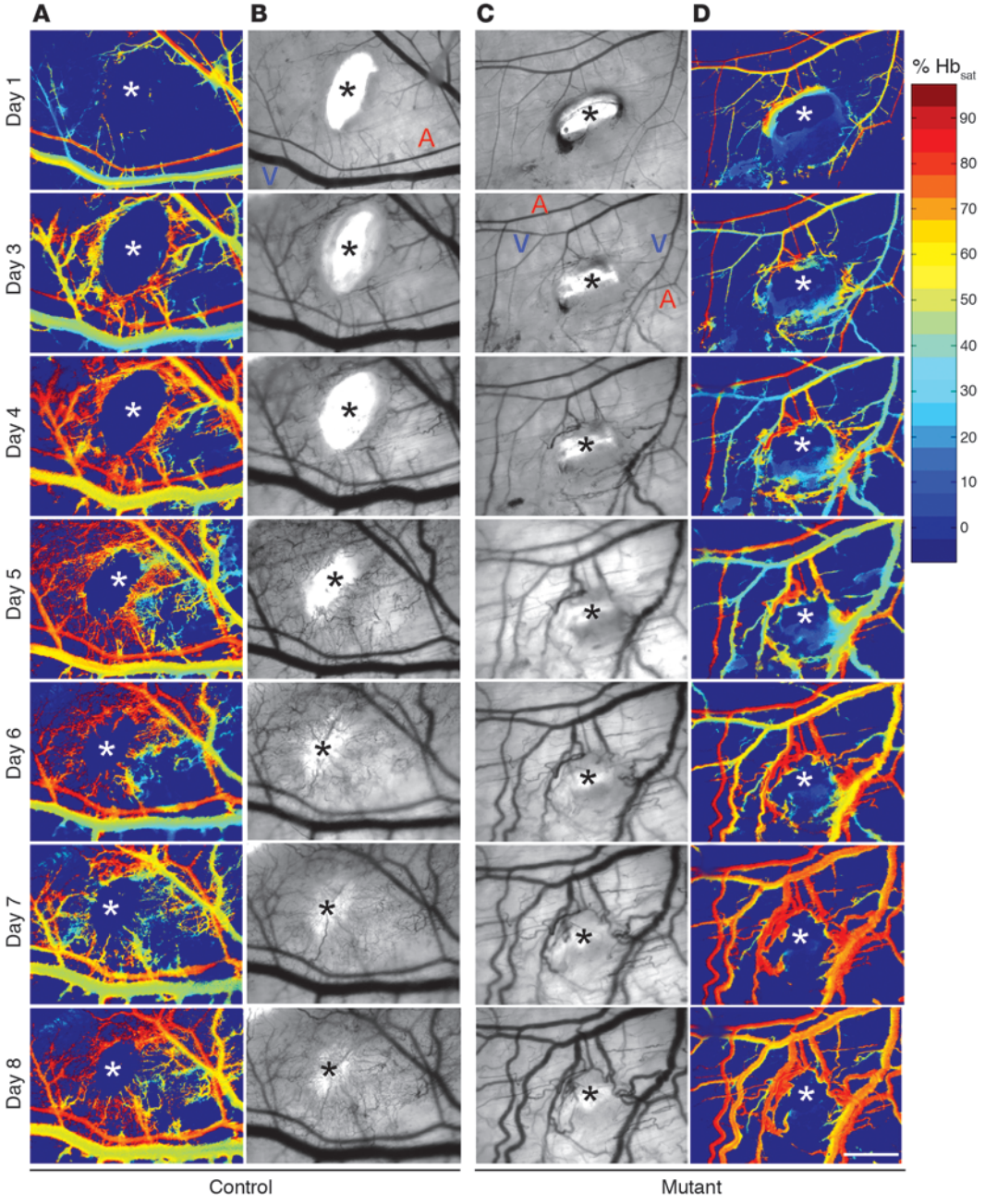

Figure 4
Intravital images of vascular morphogenesis responding to wound. The wound was induced and TM given on day 0. The center of the wound is indicated by an asterisk. Representative bright-field images of blood vessels of a control (**B**) and a mutant (**C**) mouse during wound healing for 8 days. Corresponding pseudocolor images of $Hb(O_2)$ saturation levels on the blood vessels of a control (**A**) and a mutant (**D**) mouse are shown. Arteries are distinguished from veins by their thin morphology and a high level of Hb saturation (red) at day 1. While such distinctions in major branches remained through 8 days of wound healing in controls (**A** and **B**), arteries and veins were almost indistinguishable at days 7–8 in mutant mice due to extensive remodeling and AV shunting (**C** and **D**). The color code to the right of **D** represents the percentage of $Hb(O_2)$ saturation [$Hb(O_2)_{sat}$] in the blood vessels. Scale bar (**D**, day 8): 1 mm.

process, including platelet activation, multiple cytokine activation, inflammation, matrix degradation and synthesis, angiogenesis, and recruitment of bone marrow cells (29, 30). Identification of the essential factor for AVM formation among these complex signals warrants further investigation. Based on the following observations, we speculate that active angiogenesis might be a key component of the wound response for AVM development. First, angiogenesis is an integral component of wound healing and, among the many wound responses, is the one most closely associated with vascular malformation. Second, our window chamber study showed that the wound-induced de novo AVM formation involves angiogenic processes: active extension of arterial blood

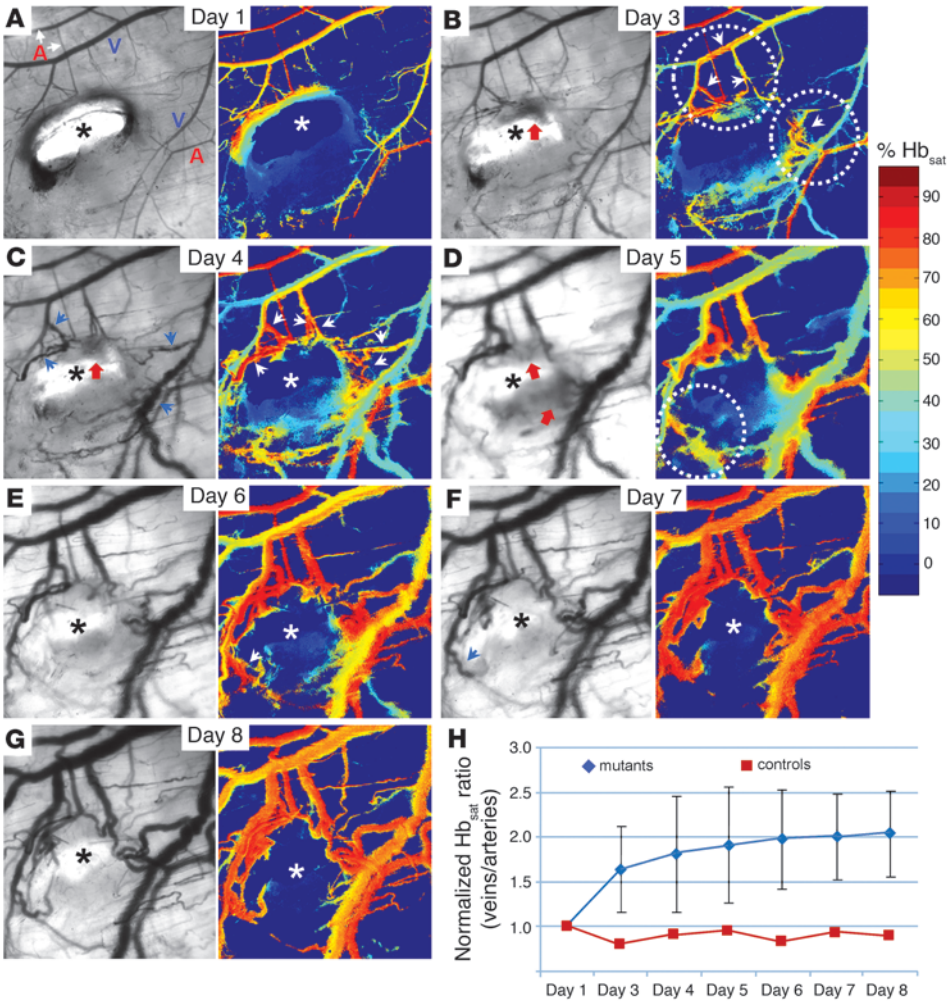

Figure 5
Vascular remodeling during development of wound-induced de novo AVM. A light-microscopic view and the corresponding Hb(O_2) pseudocolor map of vascular morphogenesis during wound healing for 8 days in the mutant. Arteries are readily distinguishable from veins by high O_2 levels days 1–5 after wounding (**A**–**D**). Early stages of AV shunts (dotted circles in **B** and **D**) were detected as early as day 3. White arrows in **B**, **C**, and **E** indicate veins containing high Hb(O_2) levels. Blue arrows in **C** and **F** indicate veins at downstream of the AV shunts, showing dilated vascular morphologies. By day 6 (**E**–**G**), Hb(O_2) levels in the veins draining from the AV shunts are as high as those in the arteries feeding to AV shunts. It is noteworthy that there were signs of bleeding where AV shunts are established (red arrows in **B**–**D**). Ratio of Hb(O_2) saturation of veins and arteries in the mutants was elevated as wound healing progressed, while that in control mice remained unchanged (**H**). Error bars in **H** indicate SD. Scale bar in **A**: 1 mm.

vessels, which meet with growing venous branches to form de novo AVM. Third, the VEGF level was shown to be elevated in the skin telangiectasis lesions of HHT patients (31, 32). Fourth, ALK1 signaling inhibits TGF-β–induced VEGF expression in ECs (33). Fifth, BMP9, a putative physiological ligand of ALK1, inhibited angiogenic activities of VEGF and bFGF in in vitro and in ovo assays (34, 35). Last, antiangiogenic drugs, such as thalidomide and bevacizumab (anti-VEGF antibody), have shown to be effective in treating GI bleeding and liver AVMs, respectively (36–38). Perhaps the effects of these antiangiogenic drugs might have come from blocking a key mediator of second hits essential for AVM development. Taken together, these data imply that ALK1 signaling may play an important role in modulating angiogenesis and is essential for organized AV connections during developmental and postnatal angiogenesis.

In this study, we showed that deletion of the *Alk1* gene from the *Alk1*^{2loxP} allele using the EC-specific L1Cre deleter line resulted in postnatal lethality (P5) with AVMs and hemorrhages in vast vascular beds of the brain, lung, and GI tract. When *Alk1* was deleted from the *Alk1*^{3loxP} allele using the same L1Cre line, the mutant mice died in late gestational periods (E17.5) (15). Since the *Alk1*^{2loxP} allele was generated from the *Alk1*^{3loxP} allele by deleting the neomycin resistant cassette flanked by the loxP sequences (15), the two conditional alleles are essentially the same. The reason why these two conditional knockouts created by using the same Cre line produce different results is unclear. Based on the fact that the vascular phenotypes of these two conditional knockout mice are essentially the same although the timing of phenotype appearance is divergent, we speculate that differences in the efficiency of Cre-mediated gene recombination between these two conditional alleles could be an underlying reason. When Cre activity was monitored in bone marrow cells of L1Cre;R26R mice, only a few cells out of thousands were X-gal positive, and Cre activity were detected almost exclusively in the vascular ECs. Taken together, these results suggest that endothelial ALK1 plays a crucial role in establishment of AV connections during vascular development.

Alk1 was shown to be expressed in arterial ECs of diverse organs (18, 39, 40), but brain, lung, and GI tract were the 3 major organs that showed obvious and consistent vascular malformations in L1Cre;*Alk1*$^{2loxP/2loxP}$ mice. This phenomenon may occur because Cre expression in the L1Cre line is much more restricted than endogenous Alk1 expression. For instance, Cre activity in internal thoracic, intercostal, and subdermal arteries in the L1Cre mice was almost undetectable, while endogenous Alk1 is expressed in those vascular beds (18). In addition, not all vascular beds where Cre was expressed (and thus Alk1 was presumably deleted) developed vascular malformation. For instance, strong Cre activity was consistently detected in glomeruli of the L1Cre mice, yet no obvious vascular malforma-

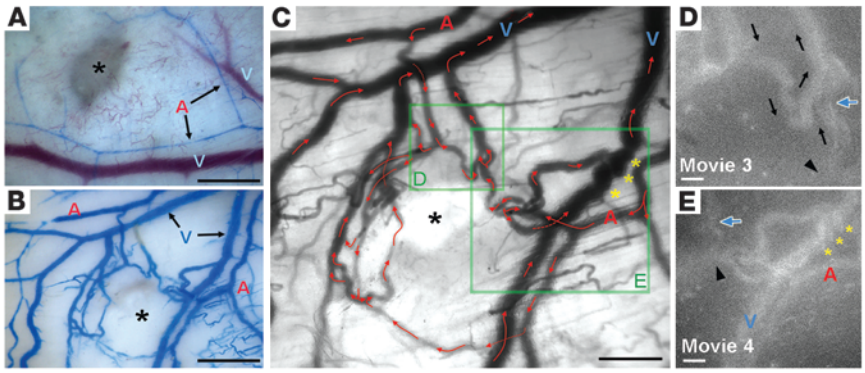

Figure 6
Blood flow through patent AV fistulas. Vascular images by latex dye injection via left heart of control (**A**) and mutant (**B**) mice demonstrate AV shunts in the mutants where latex dye was found in both arteries and veins. (**C**) Direction of blood flow obtained from video recording is indicated by arrows. Yellow asterisks indicate an area of vein at the receiving end of AV shunts showing dilated and tortuous vessel morphology. (**D** and **E**) Fluorescence images of blood flow in 2 AVM areas labeled as D and E in **C**. Black arrows in **D** indicate the direction of blood flow. Arrowheads indicate an AVM vessels showing leakage of blood. Yellow asterisks in **E** indicate a venous area having turbulent blood flow and corresponding vessel tortuosity. The blue arrows in **D** and **E** indicate the same area of blood vessel. See Supplemental Videos 3 and 4. Scale bars: 1 mm (**A** and **B**); 0.5 mm (**C**); 100 μm (**D**); 200 μm (**E**).

tion was detected in the kidney. Interestingly, the brain and lungs are two major organs where congenital forms of AVMs were often found in HHT patients. Perhaps there are some unique mechanisms of vascular development in these organs (e.g., persistent angiogenesis after birth) that make their vascular beds more susceptible to vascular malformation by ALK1 (or ENG) mutations.

The detailed molecular mechanism by which ALK1 deficiency leads to AVM formation remains to be identified. Transcriptomic and proteomic analyses of various stages of several AVM models presented here would provide valuable insights in determining the downstream targets of ALK1 signaling pertinent to AVM pathogenesis. Arteries and veins need to maintain their identities during angiogenesis to develop functional vascular networks through interactions among multiple signaling pathways. Notch/Delta signaling plays a critical role in AV specification. Notchs (Notch1, Notch4) and their ligands (Dll1 and Dll4) are expressed in arterial ECs and promote artery-specific Efnb2 expression and suppress vein-specific Ephb4 expression in arteries (41, 42). Notch loss- or gain-of-function mutants develop AVMs (24, 41, 43). Notch signaling also forms a negative feedback loop with VEGF signaling in determination of sprouting tip cells (42, 44). ALK1 is expressed in arterial ECs (18, 39), and *Alk1* deficiency results in AVM formation. Could AVM formation in ALK1-deficient vessels be due to dysregulated Notch signaling resulting in disturbance of AV specification or tip/stalk cell determination? Despite such intriguing commonalities between ALK1 and Notch signaling, little is known about the crosstalk between these two signaling pathways. The animal models presented would be invaluable for elucidating the role of crosstalk among ALK1, Notch, and VEGF signaling pathways in establishing AV connections.

Methods

Establishment of *Alk1*^{2loxP} and L1Cre lines was described previously (15). ROSA26^{CreER} mice were purchased from The Jackson Laboratory. All in vivo procedures were conducted in accordance with a protocol approved by the University of Florida Institutional Animal Care and Use Committee.

Corrosion casting and scanning electron micrography. Mice were anesthetized with i.p. injection of ketamine/xylazine (100 mg/15 mg per 1 kg body weight). The thoracic cavity was open and left or right ventricle was cannulated for perfusion with 1× PBS, 2 U of heparin for 2 minutes, followed by a corrosion resin (Mercox/methyl-methacrylate/catalyst, 8:2:0.4; Ladd Research Industries). Organs filled with resin were dissected out and immersed in hot water (50°C) for 1 hour to complete resin curing. The organ was then processed with 5% KOH maceration to form casts of bare bone, washed with distilled water, air dried, and mounted on stubs for routine scanning electron microscopy. The casts were sputter coated with platinum. The images were captured by using the Hitachi S-4000 FE-SEM, which was operated at an acceleration voltage of 6 kV.

Latex dye injection. Mice were anesthetized as described above, and abdominal and thoracic cavities were opened. For systemic vessels, both left and right atria were cut, and the latex dye (Blue latex, catalog BR80B; Connecticut Valley Biological Supply Co.) was slowly and steadily injected into the left ventricle with a glass capillary pipette for P3 mice, and with a 26-gauge 1-ml syringe needle. For pulmonary arteries, it was injected into the right heart. For pulmonary veins, only the right atrium was cut, and the dye was injected into the left ventricle. The stained samples were washed briefly in PBS and fixed with 10% formalin overnight. For whole-mount imaging, the organ or tissue of interest was dehydrated by methanol series and cleared with organic solvent (benzyl alcohol/benzyl benzoate, 1:1; Sigma-Aldrich). For P3 brains, only the head skin was peeled off before the dehydration step, but for imaging of adult brain, both skin and skull were removed.

Evans blue dye injection. Evans blue dye (0.5% in PBS without BSA) was injected via jugular vein into P3 pups anesthetized by ketamine and xylene. One hour after injection, the lung was isolated and fixed with formalin. Paraffin-embedded samples were sectioned at 7-μm thickness and then mounted with DAPI slide mounting medium (Vector Laboratories). Rhodamine and DAPI fluorescence images were captured by a Leica CTL6000 microscope and QImaging camera with OpenLab version 5.5 software (Leica Inc.).

O_2 saturation data. Oxygen saturation was measured by pulse oximeter (MouseOx; Starr Life Sciences Corp.). The mouse was placed on a restrainer without anesthesia, and the sensory clip was placed on a hind paw. The heart rate and oxygen saturation level were recorded by the software provided by the manufacturer.

Skin wound generation and image processing. The recipient mice were anesthetized by placing the animal within an induction chamber and introducing 4.0% isoflurane gas, and anesthesia was maintained by 2.0%–3.0% isoflurane. The back of the mouse was shaved and one or two 4-mm-diameter full-thickness excisional wounds were inflicted on the mid-dorsum using a biopsy punch. The wounds were left unsutured, and Betadine was applied to the wounds. No analgesics or antibiotics were given in order not to affect the wound healing process. Tamoxifen was injected i.p. at 2.5 mg/25 g of body weight on the day of wounding. The mice were anesthetized, and about 0.6 ml of latex dye was injected via left heart 7–9 days after the TM injection. After overnight fixation with formalin, the dorsal skin was peeled off. The skin was stretched, flattened, and postfixed overnight in formalin.

Hair was completely removed before dehydration in methanol and clearing. Blood vessels containing the latex dye in the cleared skin were imaged via a CCD camera. For numerical comparison to characterize blood vessels having abnormal AV shunts, the images were processed to binary images with segmentation processes including grayscale conversion, contrast adjustment, erosion and dilation, adaptive thresholding, and noise removal. The areas containing high blue channel were shown as red, while all the other areas showed black (Figure 3, E and F). This image processing technique enhanced the quality of the images and enabled us to successfully isolate the blood vessels containing the latex dye within the area of interest. All procedures were performed by using MATLAB (MathWorks Inc.).

MR microscopy for brain vascular imaging. Starting about 24 hours prior to MR microscopy, brains were washed in PBS. Immediately prior to imaging, fixed brains that had been injected with latex dye were blotted dry and then placed in a 10-mm Cryovial tube containing perfluorocarbon (FC43; 3M) for high-resolution imaging at 11.1T using a homebuilt single-tuned proton loop gap coil (internal diameter, 12 mm). High-resolution 3D-Flash images were acquired with the following parameters: FOV, 12 × 17 × 12 mm^3; matrix, 512 × 512 × 256; NEX, 2; TR/TE = 75 ms/6.3 ms; SW, 50 KHz; echo position, 30%; flip, 5°, using a Bruker spectrometer (PV3.02). Images were then converted into DICOM format, and the 3D image stack was processed using open source software (Osirix; http://www.osirix-viewer.com). With Osirix, both mutant and control brains were manually segmented on transaxial slices, and areas corresponding to low signal intensity in the brain vasculature as a consequence of the latex dye (Connecticut Valley Biological Supply Co.) were intensity thresholded and used to compute a 3D maximal intensity projection.

Dorsal skinfold chamber model. The experimental mice were anesthetized using i.p. injection of a ketamine (100 mg/kg) and xylazine (10 mg/kg) mix. The fur on the surgical site was removed with clippers, followed by 5-minute application of a depilatory cream. A titanium window chamber was surgically implanted on the dorsal skin flap. During surgery, a wound was initiated on the exposed skin area using a 16-gauge needle prick prior to placing a 12-mm-diameter no. 2 round glass coverslip over the exposed skin. Each mouse was given TM (Sigma-Aldrich) prior to surgery via an i.p. injection at 2.5 mg/25 g body weight. After surgery, animals were housed at 33°C and 50% humidity with free access to food and water and standard 12-hour light/12-hour dark cycles. All mice were imaged once every day for up to 8 days after surgery. During imaging, the animals were gas anesthetized via nose cone using isoflurane (1%–1.5%) in medical air. Anesthetized animals were maintained at 37°C by a heating pad attached to the microscope stage. A Zeiss AxioImager microscope was used as the basic platform. The long working distance objectives used were 2.5× and 5× Fluars, 10× EC Plan-Neofluar, and a 20× LD Plan-Neofluar (Zeiss).

Hyperspectral imaging. The spectral imaging system, image acquisition, and image processing methods for Hb saturation measurements were discussed in detail previously (22). For spectral information, bright-field transmitted light images were obtained using a CCD camera thermoelectrically cooled to –20°C (model 1412AM-T2-FW; DVC Company). Band-limited optical filtering was accomplished using a C-mounted liquid crystal tunable filter (LCTF) (CRI Inc.) with a 400- to 720-nm transmission range and a 10-nm nominal bandwidth, placed in front of the CCD camera (45). Hb saturation pseudocolor maps of the microvessel networks were created from the spectral image data using pure oxy- and deoxyHb reference spectra based on the method described by Shonat et al. (45).

Blood flow imaging. Real-time blood flow information was obtained on days 7 and 8 after surgery for observing the functionality of blood vessels in the experimental mice. For rbc fluorescence labeling, blood from a donor mouse was obtained via cardiac puncture. rbc were labeled with a 1 mg/ml stock solution of carbocyanine dye 1,1′-dioctadecyl-3,3,3′,3′-tetramethylindodicarbocyanine, 4-chlorobenzenesulfonate salt (DiD solid; Invitrogen, D-7757) dissolved in ethanol using a modification of the procedure by Unthank et al. (46). Briefly, the rbc were separated from whole blood by centrifugation and resuspension of the blood twice in sterile PBS. The cells were then labeled by addition of 100 μl rbc and 100 μl of DiD stock solution to 10 ml sterile PBS. The solution was incubated at room temperature for 30 minutes and agitated every 10 minutes to ensure suspension of the rbc. After labeling, the rbc were washed to remove unbound dye and resuspended in PBS. Immediately prior to an imaging session, a 50-μl bolus of packed labeled rbc in saline solution (30% v/v) was administered to the mouse to be imaged by tail vein injection. With regard to the fraction of labeled cells achieved in vivo (typically 1%–3%), it was determined from previous experiments that this protocol results in negligible absorption interference of the dye with the spectral data obtained for Hb saturation in the wavelength range employed (500–575 nm). For the rbc flow imaging system, an ANDOR iXon electron multiplying CCD (EMCCD) camera (ANDOR Technology) was used to capture streaming videos of the fluorescently labeled rbc in mouse microvasculature at a frame rate of about 30 Hz. The light source for the fluorescence imaging was a Zeiss FluoArc mercury lamp. The fluorescent rbc were observed using a Cy5 filter set (Chroma Technology Corp.; excitation: 640 nm with 20-nm bandwidth; emission: 680 nm with 30-nm bandwidth).

Statistics. Two-tailed Student's *t* test was used for statistical analysis, and a *P* value less than 0.05 was considered significant.

Acknowledgments

We thank Chul Han and Kwon-Ho Hong for technical assistance. This work was supported by NIH grant HL64024 and in part by HHT Foundation International and the World Class University project (Korean Ministry of Education, Science and Technology) to S.P. Oh; an AHA postdoctoral fellowship to S.O. Park; and NIH grant HL56921 to M.K. Raizada.

Received for publication April 8, 2009, and accepted in revised form July 29, 2009.

Address correspondence to: S. Paul Oh, Department of Physiology and Functional Genomics, University of Florida, 1376 Mowry Road, Room 456, Gainesville, Florida 32610, USA. Phone: (352) 273-8232; Fax: (352) 273-8300; E-mail: ohp@ufl.edu.

1. NIH. 2009. NINDS Arteriovenous Malformation Information Page. http://www.ninds.nih.gov/disorders/avms/detail_avms.htm.
2. Shovlin, C.L., et al. 2000. Diagnostic criteria for hereditary hemorrhagic telangiectasia (Rendu-Osler-Weber syndrome). *Am. J. Med. Genet.* **91**:66–67.
3. Abdalla, S.A., and Letarte, M. 2006. Hereditary haemorrhagic telangiectasia: current views on genetics and mechanisms of disease. *J. Med. Genet.* **43**:97–110.
4. Geisthoff, U.W., et al. 2007. Health-related quality of life in hereditary hemorrhagic telangiectasia. *Otolaryngol. Head Neck Surg.* **136**:726–733.
5. Geisthoff, U.W., Fiorella, M.L., and Fiorella, R. 2006. Treatment of recurrent epistaxis in HHT. *Curr. Pharm. Des.* **12**:1237–1242.
6. Lesnik, G.T., et al. 2007. Septectomy and septal dermoplasty for the treatment of severe transfusion-dependent epistaxis in patients with hereditary hemorrhagic telangiectasia and septal perforation. *Am. J. Rhinol.* **21**:312–315.
7. McAllister, K.A., et al. 1994. Endoglin, a TGF-beta binding protein of endothelial cells, is the gene for hereditary haemorrhagic telangiectasia type 1. *Nat. Genet.* **8**:345–351.
8. Johnson, D.W., et al. 1996. Mutations in the activin receptor-like kinase 1 gene in hereditary haemorrhagic telangiectasia type 2. *Nat. Genet.* **13**:189–195.
9. Cole, S.G., Begbie, M.E., Wallace, G.M., and Shovlin, C.L. 2005. A new locus for hereditary haemorrhagic telangiectasia (HHT3) maps to chromosome 5. *J. Med. Genet.* **42**:577–582.
10. Bayrak-Toydemir, P., et al. 2006. A fourth locus for hereditary hemorrhagic telangiectasia maps to chromosome 7. *Am. J. Med. Genet. A.* **140**:2155–2162.
11. Gallione, C.J., et al. 2004. A combined syndrome of

juvenile polyposis and hereditary haemorrhagic telangiectasia associated with mutations in MADH4 (SMAD4). *Lancet.* **363**:852–859.
12. Chang, H., Brown, C.W., and Matzuk, M.M. 2002. Genetic analysis of the mammalian transforming growth factor-beta superfamily. *Endocr. Rev.* **23**:787–823.
13. McDonald, J.E., et al. 2000. Clinical manifestations in a large hereditary hemorrhagic telangiectasia (HHT) type 2 kindred. *Am. J. Med. Genet.* **93**:320–327.
14. Sadick, H., et al. 2006. Hereditary hemorrhagic telangiectasia: an update on clinical manifestations and diagnostic measures. *Wien. Klin. Wochenschr.* **118**:72–80.
15. Park, S.O., et al. 2008. ALK5- and TGFBR2-independent role of ALK1 in the pathogenesis of hereditary hemorrhagic telangiectasia type 2 (HHT2). *Blood.* **111**:633–642.
16. Hong, K.H., et al. 2008. Genetic ablation of the BMPR2 gene in pulmonary endothelium is sufficient to predispose to pulmonary arterial hypertension. *Circulation.* **118**:722–730.
17. Badea, T.C., Wang, Y., and Nathans, J. 2003. A noninvasive genetic/pharmacologic strategy for visualizing cell morphology and clonal relationships in the mouse. *J. Neurosci.* **23**:2314–2322.
18. Seki, T., Yun, J., and Oh, S.P. 2003. Arterial endothelium-specific activin receptor-like kinase 1 expression suggests its role in arterialization and vascular remodeling. *Circ. Res.* **93**:682–689.
19. Menger, M.D., Laschke, M.W., and Vollmar, B. 2002. Viewing the microcirculation through the window: some twenty years experience with the hamster dorsal skinfold chamber. *Eur. Surg. Res.* **34**:83–91.
20. Sorg, H., Krueger, C., and Vollmar, B. 2007. Intravital insights in skin wound healing using the mouse dorsal skin fold chamber. *J. Anat.* **211**:810–818.
21. Sorg, B.S., et al. 2008. Spectral imaging facilitates visualization and measurements of unstable and abnormal microvascular oxygen transport in tumors. *J. Biomed. Opt.* **13**:014026.
22. Sorg, B.S., Moeller, B.J., Donovan, O., Cao, Y., and Dewhirst, M.W. 2005. Hyperspectral imaging of hemoglobin saturation in tumor microvasculature and tumor hypoxia development. *J. Biomed. Opt.* **10**:44004.
23. Braverman, I.M., Keh, A., and Jacobson, B.S. 1990. Ultrastructure and three-dimensional organization of the telangiectases of hereditary hemorrhagic telangiectasia. *J. Invest. Dermatol.* **95**:422–427.
24. Murphy, P.A., et al. 2008. Endothelial Notch4 signaling induces hallmarks of brain arteriovenous malformations in mice. *Proc. Natl. Acad. Sci. U. S. A.* **105**:10901–10906.
25. Croix, C.S., Zipfel, W.R., and Watkins, S.C. 2007. Potential solutions for confocal imaging of living animals. *Biotechniques.* **43**:14–19.
26. Padera, T.P., Stoll, B.R., So, P.T., and Jain, R.K. 2002. Conventional and high-speed intravital multiphoton laser scanning microscopy of microvasculature, lymphatics, and leukocyte-endothelial interactions. *Mol. Imaging.* **1**:9–15.
27. Tozer, G.M., et al. 2005. Intravital imaging of tumour vascular networks using multi-photon fluorescence microscopy. *Adv. Drug Deliv. Rev.* **57**:135–152.
28. Werkmeister, E., Kerdjoudj, H., Marchal, L., Stoltz, J.F., and Dumas, D. 2007. Multiphoton microscopy for blood vessel imaging: new non-invasive tools (Spectral, SHG, FLIM). *Clin. Hemorheol. Microcirc.* **37**:77–88.
29. Braiman-Wiksman, L., Solomonik, I., Spira, R., and Tennenbaum, T. 2007. Novel insights into wound healing sequence of events. *Toxicol. Pathol.* **35**:767–779.
30. Eming, S.A., Krieg, T., and Davidson, J.M. 2007. Inflammation in wound repair: molecular and cellular mechanisms. *J. Invest. Dermatol.* **127**:514–525.
31. Sadick, H., Naim, R., Sadick, M., Hormann, K., and Riedel, F. 2005. Plasma level and tissue expression of angiogenic factors in patients with hereditary hemorrhagic telangiectasia. *Int. J. Mol. Med.* **15**:591–596.
32. Sadick, H., Naim, R., Gossler, U., Hormann, K., and Riedel, F. 2005. Angiogenesis in hereditary hemorrhagic telangiectasia: VEGF165 plasma concentration in correlation to the VEGF expression and microvessel density. *Int. J. Mol. Med.* **15**:15–19.
33. Shao, E.S., Lin, L., Yao, Y., and Bostrom, K.I. 2009. Expression of vascular endothelial growth factor is coordinately regulated by the activin-like kinase receptors 1 and 5 in endothelial cells. *Blood*. Online publication ahead of print. doi:10.1182/blood–2009–01–199166.
34. David, L., et al. 2008. Bone morphogenetic protein-9 is a circulating vascular quiescence factor. *Circ. Res.* **102**:914–922.
35. Scharpfenecker, M., et al. 2007. BMP-9 signals via ALK1 and inhibits bFGF-induced endothelial cell proliferation and VEGF-stimulated angiogenesis. *J. Cell Sci.* **120**:964–972.
36. Kurstin, R. 2002. Using thalidomide in a patient with epithelioid leiomyosarcoma and Osler-Weber-Rendu disease. *Oncology (Williston Park).* **16**:21–24.
37. Perez-Encinas, M., Rabunal Martinez, M.J., and Bello Lopez, J.L. 2002. Is thalidomide effective for the treatment of gastrointestinal bleeding in hereditary hemorrhagic telangiectasia? *Haematologica.* **87**:ELT34.
38. Mitchell, A., et al. 2008. Bevacizumab reverses need for liver transplantation in hereditary hemorrhagic telangiectasia. *Liver Transpl.* **14**:210–213.
39. Seki, T., Hong, K.H., Yun, J., Kim, S.J., and Oh, S.P. 2004. Isolation of a regulatory region of activin receptor-like kinase 1 gene sufficient for arterial endothelium-specific expression. *Circ. Res.* **94**:e72–e77.
40. Seki, T., Hong, K.H., and Oh, S.P. 2006. Nonoverlapping expression patterns of ALK1 and ALK5 reveal distinct roles of each receptor in vascular development. *Lab. Invest.* **86**:116–129.
41. Gridley, T. 2007. Notch signaling in vascular development and physiology. *Development.* **134**:2709–2718.
42. Roca, C., and Adams, R.H. 2007. Regulation of vascular morphogenesis by Notch signaling. *Genes Dev.* **21**:2511–2524.
43. Carlson, T.R., et al. 2005. Endothelial expression of constitutively active Notch4 elicits reversible arteriovenous malformations in adult mice. *Proc. Natl. Acad. Sci. U. S. A.* **102**:9884–9889.
44. Hellstrom, M., et al. 2007. Dll4 signalling through Notch1 regulates formation of tip cells during angiogenesis. *Nature.* **445**:776–780.
45. Shonat, R.D., Wachman, E.S., Niu, W., Koretsky, A.P., and Farkas, D.L. 1997. Near-simultaneous hemoglobin saturation and oxygen tension maps in mouse brain using an AOTF microscope. *Biophys. J.* **73**:1223–1231.
46. Unthank, J.L., Lash, J.M., Nixon, J.C., Sidner, R.A., and Bohlen, H.G. 1993. Evaluation of carbocyanine-labeled erythrocytes for microvascular measurements. *Microvasc. Res.* **45**:193–210.